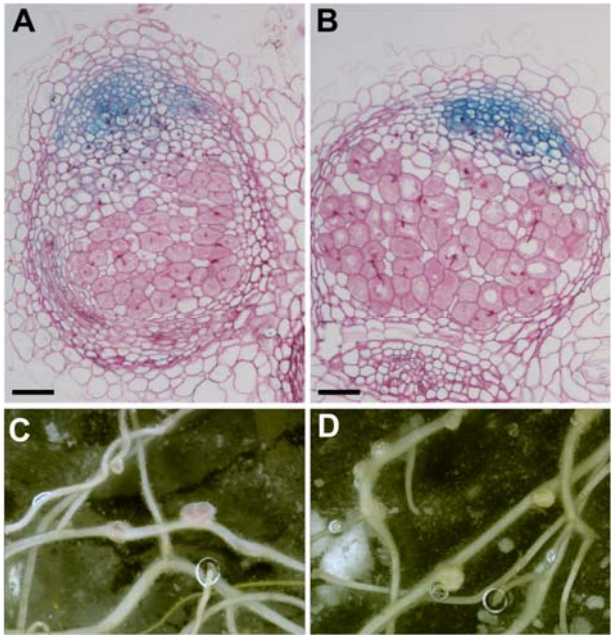

Supplemental Figure 1: Biological activity of the LYK3 and NFP fluorescent fusion constructs. (A) Nodule expressing pLYK3:GUS construct. Bar is 75 µm. (B) Nodule expressing pNFP:GUS construct. Bar is 75 µm. (C) Complementation of the B56 mutant with pLYK3:LYK3-GFP restores nodulation. (D) Complementation of the NFP31 mutant with pNFP:NFP-GFP restores nodulation.

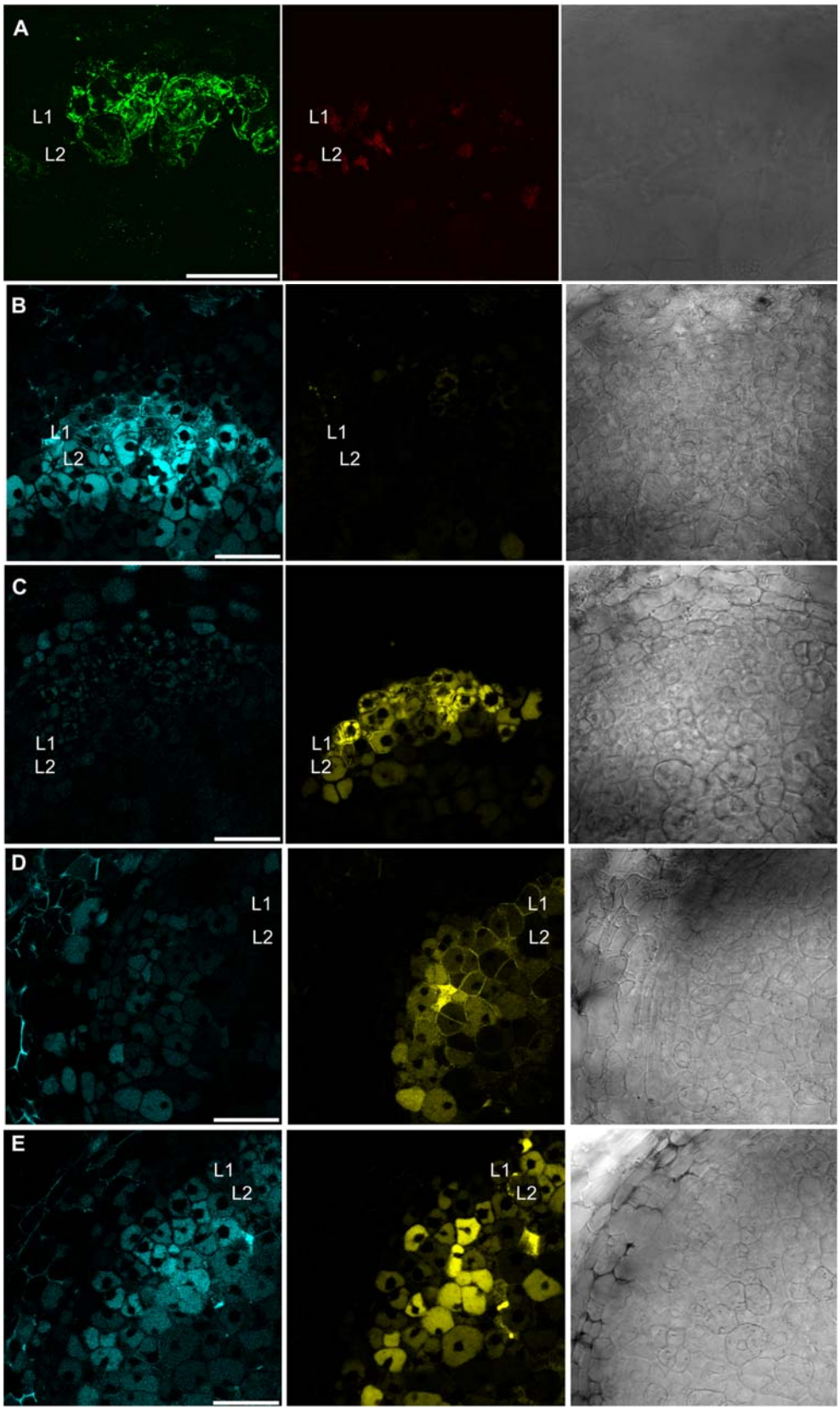

Supplemental Figure 2: Accumulation of LYK3 and NFP in the nodule apex. (A) LYK3-GFP in *pLYK3:LYK3-GFP* expressing nodule detected with an anti-GFP antibody. (B) (from left to right) cyan

fluorescence intensity, yellow autofluorescence intensity, and DIC images of a *pLYK3:LYK3-mTQ2* expressing nodule. (C) (from left to right) cyan autofluorescence intensity, yellow fluorescence intensity, and DIC images of a *pLYK3:LYK3-Venus* expressing nodule. (D) (from left to right) cyan autofluorescence intensity, yellow fluorescence intensity, and DIC images of a *pNFP:NFP-Venus* expressing nodule. (E) (from left to right) cyan fluorescence intensity, yellow fluorescence intensity, and DIC images of a *pLYK3:LYK3-mTQ2* and *pNFP:NFP-Venus* co-expressing nodule. (A,B,C,D,E) Bar is 50 µm.

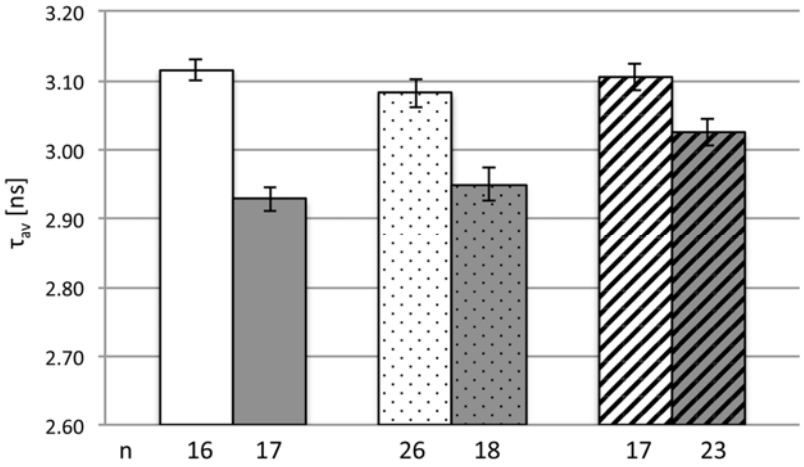

Figure 3: NFP and LYK3 oligomerization at the plasma membrane in *Nicotiana* leaf epidermal cells. Lifetime (τ_{av}) measurements in leaves (co-)expressing LYK3-sYFP2 (white), LYK3-sYFP2+LYK3-mCherry (grey), NFP-sYFP2 (white dotted), NFP-sYFP2+NFP-mCherry (grey dotted), NFP-sYFP2 (white hatched), and NFP-sYFP2+LYK3 G334E-mCherry (grey hatched) (NFP homomerization and NFP heteromerization with LYK3 G334E were studied on different days, and therefore they use different donor only-control measurements). Columns present median τ_{av} from at least two experiments. Bars represent confidence intervals at confidence level = 0.05. n is number of measurements.

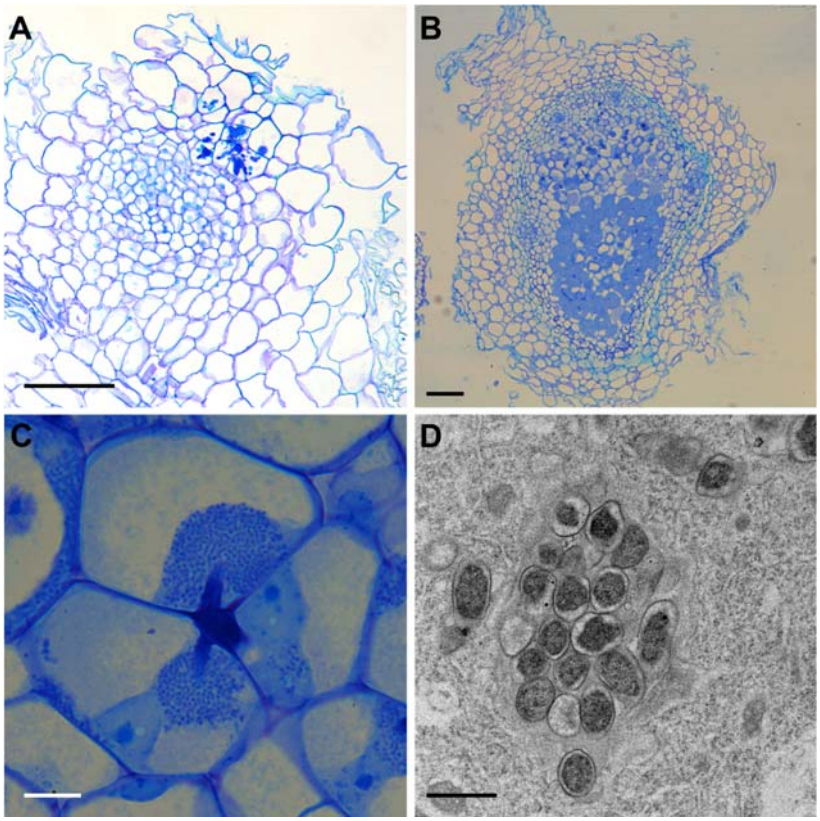

Figure 4: Phenotypes of *LYK3* knock down in nodules 21 dpi.

The nodule apex is located at the top of the images. (A) Nodule of the *lyk3-1* mutant expressing LYK3 under control of the epidermis specific *EXT1* promoter in which the infection thread could not enter and development stopped. (B,C,D) Nodule expressing a *LYK3* RNAi hairpin in a nodule specific manner (*pENOD12:LYK3* RNAi). These nodules have very large unwalled droplets from which bacteria are eventually released. (D) electron micrograph of such an unwalled droplet confirming that the plant cell wall is not present (A,B) Bar is 100 µm. (C) Bar is 10 µm. (D) Bar is 1 µm.

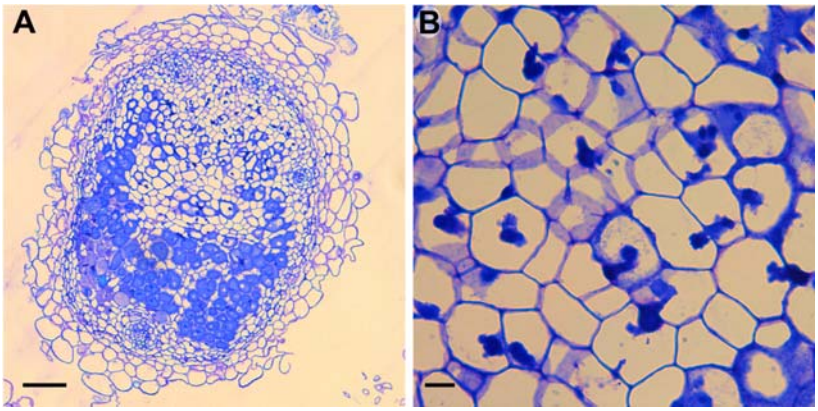

Figure 5: Ectopic expression of LYK3 in nodules 21 dpi.

(A,B) Nodule expressing *pUbq:LYK3* in which infection threads can penetrate the cells but bacteria are not released. (A) Bar is 100 µm, (B) Bar is 10 µm.

Supplemental Table 1. Entry constructs

Construct	Primers	Plasmid backbone	Cloning method
pENTR pNFP	CACCGTGCCTAGAGTCAACCATTGG	pENTR™/D-TOPO® (Invitrogen)	TOPO ligase
	CATGCTCGAGAAGAGAAAAGAGAGTTTCTTATGGCA		
pENTR pLYK3	TTCACCGGACAGATAGCGCAG		
	TGTATCAAGAAGAGAGAGAGAAAGAGAA		
pENTR pNFP:NFP	CACCGTGCCTAGAGTCAACCATTGG		
	ACGAGCTATTACAGAAGTAACAACA		
pENTR NFP	CACCATGTCTGCCTTCTTTCTTCC		
	ACGAGCTATTACAGAAGTAACAACA		
pENTR pLYK3:LYK3	TTCACCGGACAGATAGCGCAG		
	TCTAGTTGACAACAGATTTATGAGAGA		
pENTR LYK3	CACCACAATATTGTATTGGTGAGATCATATAAGA		
	TCTAGTTGACAACAGATTTATGAGAGA		
pENTR23 mTQ2	-	pENTR-p2rp3-MCS-Stop-T35S (Ovchinnikova et al., 2012)	AscI, KpnI
pENTR23 Venus	-		

Supplemental Table 2. Destination constructs

Use	Construct	pENTR p4p1r	pENTR 12	pENTR p2rp3	pDEST	Cloning method
Promoter GUS	pNFP:GUS RR	-	pENTR pNFP	-	pKGWFS7 RR (Karimi et al., 2002)	LR clonase II (Invitrogen)
	pLYK3:GUS RR	-	pENTR pLYK3	-		
Ectopic expression	pUbq:NFP-GFP RR	-	pENTR NFP	-	pUbq pK7WGF2-RR (Limpens et al., 2009)	
	pUbq :LYK3-GFP RR	-	pENTR LYK3	-		
RNAi	pENOD12:NFP RNAi	-	pENTR NFP	-	pE12 pK7GWIWG2(II) (Limpens et al., 2005)	
	pENOD12 :LYK3 RNAi	-	pENTR LYK3	-		
Localization FRET-FLIM	pNFP :NFP-GFP	pENTR41 (empty)	pENTR pNFP :NFP	pENTR23 eGFP (Ovchinnikova et al., 2012)	pKGW-RRMGW (Ovchinnikova et al., 2012)	LR Clonase II plus (Invitrogen)
	pNFP :NFP-RFP	pENTR41 (empty)	pENTR pNFP :NFP	pENTR23 mCherry (Ovchinnikova et al., 2012)	pKGW-MGW (Ovchinnikova et al., 2012)	
	pNFP :NFP-mTQ2	pENTR41 (empty)	pENTR pNFP :NFP	pENTR23 mTQ2		
	pNFP :NFP-Venus	pENTR41 (empty)	pENTR pNFP :NFP	pENTR23 Venus		
	pLYK3 :LYK3-GFP	pENTR41 (empty)	pENTR pLYK3 :LYK3	pENTR23 eGFP (Ovchinnikova et al., 2012)	pKGW-RRMGW (Ovchinnikova et al., 2012)	
	pLYK3: LYK3-mTQ2	pENTR41 (empty)	pENTR pLYK3 :LYK3	pENTR23 mTQ2	pKGW-MGW (Ovchinnikova et al., 2012)	
	pLYK3: LYK3-Venus	pENTR41 (empty)	pENTR pLYK3 :LYK3	pENTR23 Venus		
	pRR	-	-	-	pKGW-RRMGW (Ovchinnikova et al., 2012)	

Supplemental Methods

Testing biological activity of tagged proteins

The promoter regions of both genes were fused to GUS and the resulting binary contruct was transformed in Medicago A17. The GUS pattern was compared to *in situ* hybridization and promoter: *GUS* analysis (Limpens et al., 2005; Arrighi et al., 2006; Haney et al., 2011). To test whether these fusion constructs are functional, they were introduced into the corresponding mutant background: the *nfp-1* mutant C31 (Arrighi et al., 2006) for *NFP* constructs, and the *lyk3-1* mutant B56 (Smit et al., 2007) for *LYK3* constructs. Upon inoculation with *Sinorhizobium meliloti,* nodule number were compared to plants transformed with a control vector.

Immuno-localization of LYK3-GFP in thick sections

Transgenic roots and nodules were selected based on DsRED1 expression using a Leica MZFLIII binocular fitted with a HQ553/30 optical filter (Leica Microsystems, Rijswijk, The Netherlands). Nodules where fixed for 1 hour in 1% paraformaldehyde and washed three times in PBS. The nodules were cut in half longitudinally and incubated over night with polyclonal rabbit anti-GFP antibodies (Molecular Probes) in dilution 1:200 at 4°C. Goat anti-Rabbit antibodies (Molecular Probes) coupled to Alexa488 where used as a second antibody (1:200 dilution). Nodules were examined on a Zeiss LSM 510 confocal laser scanning microscope (Carl-Zeiss Axiovert [Oberkochen, Germany] 200 M equipped with a 488 nm argon laser line. The light was guided via a HFT 488 primary dichroic mirror, through an oil immersed 40x Plan-Neofluar objective (NA 1.3) into the sample. Emission was guided via a NFT 545 dichroic mirror and GFP emission was selectively detected using a 505 to 530 nm BP filter.

Global fitting and phasor analysis of time resolved FLIM data

Fractions and lifetimes where obtained by globally fitting control and FRET sample decay curves simultaneously. We considered FRET samples as mixtures of non-FRETting (free and/or homocomplexed) and FRETting donor fusion proteins. Only one global lifetime (τ_D) was used for the donor only-control measurements, and two global lifetimes (τ_D and τ_{DA}) were used for FRET sample measurements, where τ_{DA} represents the donor τ in the FRETting state.

Because the photon counts, I, were very low in the tail for the small regions of interest analyzed in the image we optimized the Poissonian loglikelihood function (MLE), $L = \sum_k \sum_t h_{k,t} - I_{k,t} \ln\left(h_{k,t}\right)$ using a modified Levenberg-Marquardt algorithm (Barber et al., 2005; Barber et al., 2009) implemented in Matlab.

Decay curves modeled using a single or a sum of two exponential functions were reconvolved with the instrument response function, $IRF(t\text{-}t')$. The IRF estimated based on the whole image was obtained from the SymphoTime software, and area normalized. The general model for single or double decay curves, $h_k(t)$, measured with bin size Δt = 16 ps was:

$$h_k\left(t\right) = b_k + IRF_k\left(t - t_k^{'}\right) \otimes \sum_i a_{k,i} \Delta t \exp\left(-t/\tau_i\right)/\tau_i \ ,$$

where b_k denotes the local background parameter, $a_{k,i}$ denotes the local amplitude parameter in total photon counts for component i, and τ_i denotes the global lifetime of component i. All parameters,

including the local IRF time shift parameter, t_k' were directly obtained from the global fit. In order to ensure correct estimation of lifetime component fractions, $f_{1,2} = a_{1,2}/(a_1+a_2)$ the whole time range of the decay curve from 0-50 ns was used in the fit. Confidence intervals for lifetimes and median fraction values were estimated by the method of bootstrapping. From each control and FRET sample dataset, a random control and FRET sample dataset with replacement was obtained and fitted again. From 250 bootstrap samples the empirical 2.5% and 97.5% percentile was used as an estimate of the confidence interval.

The time-resolved τ of mTQ2 measured in the membrane environment ranges between 3.90 and 4.00 ns (M. H. – personal communication). The decrease from the mTQ2 measured *in vitro*, 4.33 ns, is due to differences in the refractive index. The apparent FRET efficiency (E_{app}) values for the FRET-FLIM data from Medicago can be calculated as follows:

$$E_{app} = \left(1 - \frac{f_D \tau_D + f_{DA} \tau_{DA}}{\tau_D}\right) \times 100\% \qquad \text{(Eq. 1)}$$

The decay curves were also analyzed using the phasor approach (Digman et al., 2008; Fereidouni et al., 2011). In order to obtain the estimate phasor of the pure fluorescence decay component in the measured decay curves we calculated the (third harmonic) phasor of each background subtracted decay curve, which was divided by the (third harmonic) phasor of the instrument response function. The IRFs were first shifted with the fitted time shift parameter, t_k'. A disk shaped weighted smoothing filter (filter diameter 5 pixels and weighted with total counts per intensity pixel) was applied on the phasor images, and the resulting smoothed lifetime image was visualized as a false color image, where the intensity of the false color of each pixel was adjusted to match the intensity of the unsmoothed fluorescence intensity image. The complex phasor points, $p_h = g_h(\omega) + i \cdot s_h(\omega)$ were calculated using the cosine and sine transform:

$$g_h(\omega) = \frac{\sum_j \cos(\omega \cdot t_j) h_j'}{\sum_j h_j'},\ s_h(\omega) = \frac{\sum_j \sin(\omega \cdot t_j) h_j'}{\sum_j h_j'}$$

Where h'_j denotes the background corrected decay curve and ω the angular frequency, $\omega = 2\pi n / T$. We used the third harmonic $n = 3$ and the sample period was $T = 50$ ns, yielding an angular frequency of $\omega = 0.377$ rad·ns^{-1}. We removed the effect of the IRF by dividing the complex phasor points (from the decay curves) by the complex phasor point of the IRF using the same angular frequency, as follows: $p_h'(\omega) = p_h(\omega) / p_{IRF}(\omega)$. Apparent lifetimes τ_φ and τ_M based on phasor points were calculated as follows:

$$\tau_\phi(\omega) = \frac{1}{\omega}\frac{s(\omega)}{g(\omega)},\ \tau_M(\omega) = \frac{1}{\omega}\sqrt{\frac{1}{g^2(\omega)+s^2(\omega)} - 1}$$

The average lifetime from phasor points was calculated as $\tau_{av}(\omega) = \sqrt{\tau_\phi(\omega)\tau_M(\omega)}$.

Confocal microscopy and Fluorescence Correlation Spectroscopy Setup

Measurements were performed on an inverted Fluoview 1000 laser scanning microscope (Olympus). The excitation light of a 440 nm 20 MHz pulsing laser diode (Picoquant), as controlled by a SepiaII

laser driver unit (Picoquant), was attenuated 10 times by a neutral density filter. The light was guided via a D440/514/594 primary dichroic mirror (Chroma) through a water immersed 60x UPlanS-Apo objective (NA 1.2) into the sample. For calibration purposes purified solutions of mTurquoise2 in PBS buffer were measured in glass-bottomed 96-wells chambers (Greiner). The emission light was guided via a size-adjustable pinhole, set at 120 µm, either to the internal photomultiplier combined with a 455-500 bandpass filter or via an optical fiber to the a custom-made detection box (Picoquant) containing PDM avalanche photodiodes (MPD). Here the light was guided into one of the MPDs and filtered by a 475/42 emission filter (Chroma). The photon arrival times were recorded by a Picoharp 300 time-correlated single-photon counting system (Picoquant).

Confocal intensity measurements

The photons were collected for an 512x512 pixels sized image by the Fluoview (v4.1) (Olympus) software. Acquisition settings of 12.5 us/pixel, zoomfactor 3, PMT sensitivity at 900V, PMT gain 1 and PMT offset of 35 were fixed for all acquired images. The intensity of the 440 nm laser line (5.6 µW/cm^2) was identical to the sequentially acquired FCS measurements.

Fluorescence Correlation Spectroscopy measurements

The photon arrival times were recorded during 120-240 seconds by the SymPhoTime 64 (v1.6) (Picoquant) software. The size and shape of the observation volume was determined from FCS calibration measurements using purified mTQ2 as outlined in Maeder et al. (2007). The diffusion time of the fusion proteins was analysed by FCS fitting in FFS Data Processor 2.3 software (SSTC). Sections of raw data, lacking significant photobleaching and aggregation spikes, were autocorrelated and analyzed using a one-component 3D diffusion model with correction for triplet/blinking kinetics (Hink, 2014)

$$G(\tau) = 1 + \frac{\gamma}{N} \cdot \left(\frac{1 - T + Te^{\frac{-\tau}{\tau_{TRIP}}}}{(1-T)} \cdot \frac{1}{\left(1 + \frac{\tau}{\tau_{dif}}\right)\sqrt{1 + \frac{\tau}{sp^2 \tau_{dif}}}} \right) \qquad \text{Eq. 2}$$

The autocorrelation function, *G(τ)*, scales to the average number of fluorescent particles in the detection volume, *N*. τ_{dif} denotes the average diffusion time of the fluorescent molecules, *T* corresponds to the fraction of molecules present in the dark state and τ_{TRIP} is the average time a molecule resides in the dark state. Parameter *γ* represents the geometric scaling factor of the detection volume and equals 1 when approximating the volume to be cylinder-like. By fitting the autocorrelation curve a shape factor, *sp*, can be obtained that describes the ratio of the axial (ω_z) over the lateral (ω_{xy}) e^{-2} radius of the detection volume. Here the volume was estimated from a calibration measurement of purified mTQ2 in PBS buffer, having a known diffusion coefficient, *D*, of 90 10^{-12} m^2*s^{-1} and using the following equations:

$$\tau_{dif} = \frac{\omega_{xy}^{2}}{4D} \quad \text{(Eq. 3)}$$

$$V = 2 \cdot \pi \cdot \mathrm{sp} \cdot \omega_{xy}^{3} \quad \text{(Eq. 4)}$$

To improve fitting speed and quality, the parameters were constrained to be minimal 100 µs for τ_{dif} and maximal 100 µs for τ_{TRIP}. The obtained particle number, *N*, was converted into a molar concentration using the estimated volume of 0.4 10^{-15} liter, via equation 4.

Concentration estimation from FCS and confocal imaging measurements

A titration series of purified mTQ2 in PBS was acquired sequentially by both confocal microscopy as FCS. Fitting of the FCS curves retrieved the molar concentrations in these solutions. The fluorescence signal observed in each confocal image is originating from the amount of mTQ2 present in the same detection volume as is observed in the corresponding FCS measurement. The measured concentration (FCS) was plotted versus the observed image intensity (confocal) for the nano- & low micro-molar concentration range. This calibration curve was linear extrapolated for higher confocal image intensities where FCS measurements could not be performed.

To convert the confocal image intensities in the Medicago nodule cells into protein densities, the intensity at the cell periphery was converted into a concentration value using the calibration curve described above. However, in this case the fluorescence is originating from a small, more or less flat, piece of membrane instead of a homogeneous solution as used for the calibration curve. In most cases the measured membranes were orientated along the x-z axis of the microscope (see Figure 5a,b,c for examples of ROIs). Therefore, the estimated concentration, as measured in 0.4 femtoliter, was in fact originating from a flat elipse with a surface of $\pi^*\omega_{xy}^*\omega_z$ (here π*220 nm*1320 nm). The calibration measurements were used to estimate molar concentrations in ROIs that: 1) were included in the FRET-FLIM analyses, 2) could be attributed to a single cell expressing the mTQ2 fusion (boundary regions between two mTQ2 expressing cells were not taken into consideration). By inserting Avogadro's number the measured confocal intensity can be converted to protein density:

protein density (molecules/nm^2) = concentration$_{\text{calibration curve}}$ (mol/liter) * 0.4 10^{-15} (liter) * 6.02 10^{23} (molecules/mol) / (π*220*1320) (nm^2) (Eq. 5)

This results in a typical protein density of 2.7 10^{-4} molecules per nm^2.

Nicotiana transformations

The pBin+ CaMV 35S:*NFP-sYFP2* or *-mCherry*, pCambia1390 CaMV 35S:*LYK3-sYFP2* or *-mCherry*, and pCambia1390 CaMV 35S:*LYK3 G334E-mCherry* constructs are described (Pietraszewska-Bogiel et al., 2013). Transformation of *A. tumefaciens* strain GV3101:pMP90 and *Agrobacterium*-mediated transient transformation of *N. benthamiana* leaves is described (Pietraszewska-Bogiel et al., 2013). *Agrobacterium* transformants carrying the respective construct were resuspended in the infiltration

medium to desired OD_{600}: *NFP* constructs – OD_{600} between 0.1 and 0.3; *LYK3* and *LYK3 G334E* constructs – OD_{600} between 0.5 and 0.7. Subsequently, *Agrobacterium* transformants carrying a desired construct fused to *sYFP2* were mixed 1:1 with *Agrobacterium* transformants carrying an empty pCambia1390 vector (for the donor only-control) or a desired construct fused to *mCherry* (for the FRET sample) before being infiltrated into Nicotiana leaves. FRET-FLIM analyses in leaf samples (co-)expressing *NFP-sYFP2* and *NFP-mCherry* constructs or *LYK3 G334E-sYFP2* and *NFP-mCherry* constructs were performed not sooner than 36 hai; in those (co-)expressing *LYK3* constructs – between 24-36 hai.

FRET-FLIM imaging and data analysis in Nicotiana

Leaf fragments were mounted on microscope slides in water and further analyzed on a wide-field Zeiss (Carl-Zeiss Axiovert [Oberkochen, Germany]) 200 M equipped with a 514 nm argon laser line (Melles Griot). The light was guided through an oil immersed 40x Plan-Neofluar objective (NA 1.3) into the sample. YFP emission was selectively detected using 542/27 and 525 LP filters (Chroma). Post-acquisition, an intensity threshold was applied to each region of interest in order to calculate τ_φ and τ_M . The average lifetime in a ROI was calculated as $\tau_{av} = \sqrt{\tau_\phi \tau_M}$. The E_{app} was calculated as

$$E_{app} = 1 - \frac{\tau_{av}}{\tau_D}$$

During each FRET-FLIM experiment, at least 5 independent τ images were acquired; exposition times for the donor only-control and FRET samples were kept constant or similar, and generally were 100-200 ms per τ image. Each FRET experiment was repeated at least twice (usually three times).

Estimating the significance of bystander FRET in FRET-FLIM measurements

Because the LYK3/NFP expressing cells were imaged on sections through nodules, and not via deep tissue imaging (in fact, the cells with visible LYK3/NFP accumulation were likely located in the immediate vicinity of the cover glass), fluorescence scatter was insignificant in our samples. Therefore, fluorescence intensity measurements in this case should (relatively) accurately estimate molar concentrations of fluorescent fusions. The molar concentrations were estimated for the mTQ2 fusions, as this fluorescent protein shows superior photobleaching stability to Venus. The molecular concentrations of LYK3 in our samples was calculated using equation 5. We speculate that the molecular concentration of LYK3-Venus fusion was similar, and that it was considerably higher than that of NFP-Venus fusion. The maximal bystander FRET (in a situation where the donor fusions are present as monomers, and the distance of the closest donor-acceptor approach is minimal and equals 2*radius of the fluorescent protein β-barrel [2.6 nm]) was calculated for the acceptor concentrations measured according to equation 3 and 4 (Fung and Stryer, 1978); Förster radius, R_0, for mTQ2-Venus pair is 5.83 nm (Goedhart et al., 2012)).

Supplemental references

Arrighi, J.F., Barre, A., Ben Amor, B., Bersoult, A., Soriano, L.C., Mirabella, R., de Carvalho-Niebel, F., Journet, E.P., Gherardi, M., Huguet, T., Geurts, R., Denarie, J., Rouge, P., and Gough, C. (2006). The Medicago truncatula lysin motif-receptor-like kinase gene family includes NFP and new nodule-expressed genes. Plant physiology **142,** 265-279.

Barber, P.R., Ameer-Beg, S.M., Gilbey, J.D., Edens, R.J., Ezike, I., and Vojnovic, B. (2005). Global and pixel kinetic data analysis for FRET detection by multi-photon time-domain FLIM. In Multiphoton Microscopy in the Biomedical Sciences V, A. Periasamy and P.T. So, eds, pp. 171-181.

Barber, P.R., Ameer-Beg, S.M., Gilbey, J.D., Carlin, L.M., Keppler, M., Ng, T.C., and Vojnovic, B. (2009). Multiphoton time-domain fluorescence lifetime imaging microscopy: practical application to protein–protein interactions using global analysis. J. R. Soc. Interface **6,** S93–S105.

Digman, M.A., Caiolfa, V.R., Zamai, M., and Gratton, E. (2008). The phasor approach to fluorescence lifetime imaging analysis. Biophysical journal **94,** L14-16.

Fereidouni, F., Esposito, A., Blab, G.A., and Gerritsen, H.C. (2011). A modified phasor approach for analyzing time-gated fluorescence lifetime images. Journal of microscopy **244,** 248-258.

Haney, C.H., Riely, B.K., Tricoli, D.M., Cook, D.R., Ehrhardt, D.W., and Long, S.R. (2011). Symbiotic Rhizobia Bacteria Trigger a Change in Localization and Dynamics of the Medicago truncatula Receptor Kinase LYK3. The Plant cell **23,** 2774-2787.

Hink, M.A. (2014). Quantifying intracellular dynamics using fluorescence fluctuation spectroscopy. Protoplasma **251,** 307-316.

Karimi, M., Inze, D., and Depicker, A. (2002). GATEWAY vectors for Agrobacterium-mediated plant transformation. Trends in plant science **7,** 193-195.

Limpens, E., Ivanov, S., van Esse, W., Voets, G., Fedorova, E., and Bisseling, T. (2009). Medicago N2-fixing symbiosomes acquire the endocytic identity marker Rab7 but delay the acquisition of vacuolar identity. The Plant cell **21,** 2811-2828.

Limpens, E., Mirabella, R., Fedorova, E., Franken, C., Franssen, H., Bisseling, T., and Geurts, R. (2005). Formation of organelle-like N2-fixing symbiosomes in legume root nodules is controlled by DMI2. Proceedings of the National Academy of Sciences of the United States of America **102,** 10375-10380.

Maeder, C.I., Hink, M.A., Kinkhabwala, A., Mayr, R., Bastiaens, P.I., and Knop, M. (2007). Spatial regulation of Fus3 MAP kinase activity through a reaction-diffusion mechanism in yeast pheromone signalling. Nature cell biology **9,** 1319-1326.

Ovchinnikova, E., Journet, E.P., Chabaud, M., Cosson, V., Ratet, P., Duc, G., Fedorova, E., Liu, W., den Camp, R.O., Zhukov, V., Tikhonovich, I., Borisov, A., Bisseling, T., and Limpens, E. (2012). IPD3 controls the formation of nitrogen-fixing symbiosomes in pea and Medicago Spp. Mol Plant Microbe Interact **24,** 1333-1344.

Smit, P., Limpens, E., Geurts, R., Fedorova, E., Dolgikh, E., Gough, C., and Bisseling, T. (2007). Medicago LYK3, an entry receptor in rhizobial nodulation factor signaling. Plant physiology **145,** 183-191.